

A MASSIVE MOLECULAR GAS RESERVOIR IN THE $Z = 2.221$ TYPE-2 QUASAR HOST GALAXY SMM J0939+8315 LENSED BY THE RADIO GALAXY 3C220.3

T. K. DAISY LEUNG AND DOMINIK A. RIECHERS

Department of Astronomy, Space Sciences Building, Cornell University, Ithaca, NY 14853, USA; tleung@astro.cornell.edu

Accepted to the ApJ

ABSTRACT

We report the detection of CO($J = 3 \rightarrow 2$) line emission in the strongly-lensed submillimeter galaxy (SMG) SMM J0939+8315 at $z = 2.221$, using the Combined Array for Research in Millimeter-wave Astronomy. SMM J0939+8315 hosts a type-2 quasar, and is gravitationally lensed by the radio galaxy 3C220.3 and its companion galaxy at $z = 0.685$. The 104 GHz continuum emission underlying the CO line is detected toward 3C220.3 with an integrated flux density of $S_{\text{cont}} = 7.4 \pm 1.4$ mJy. Using the CO($J = 3 \rightarrow 2$) line intensity of $I_{\text{CO}(3-2)} = (12.6 \pm 2.0)$ Jy km s⁻¹, we derive a lensing- and excitation-corrected CO line luminosity of $L'_{\text{CO}(1-0)} = (3.4 \pm 0.7) \times 10^{10} (10.1/\mu_L)$ K km s⁻¹ pc² for the SMG, where μ_L is the lensing magnification factor inferred from our lens modeling. This translates to a molecular gas mass of $M_{\text{gas}} = (2.7 \pm 0.6) \times 10^{10} (10.1/\mu_L) M_{\odot}$. Fitting spectral energy distribution models to the (sub)-millimeter data of this SMG yields a dust temperature of $T = 63.1_{-1.3}^{+1.1}$ K, a dust mass of $M_{\text{dust}} = (5.2 \pm 2.1) \times 10^8 (10.1/\mu_L) M_{\odot}$, and a total infrared luminosity of $L_{\text{IR}} = (9.1 \pm 1.2) \times 10^{12} (10.1/\mu_L) L_{\odot}$. We find that the properties of the interstellar medium of SMM J0939+8315 overlap with both SMGs and type-2 quasars. Hence, SMM J0939+8315 may be transitioning from a star-bursting phase to an unobscured quasar phase as described by the “evolutionary link” model, according to which this system may represent an intermediate stage in the evolution of present-day galaxies at an earlier epoch.

Subject headings: cosmology: observations — galaxies: evolution — galaxies: high-redshift — galaxies: starburst — submillimeter: galaxies

1. INTRODUCTION

Submillimeter-selected galaxies (SMGs) are predominantly found at redshifts $z \sim 1 - 3$ (Chapman et al. 2005), during the epoch of stellar mass and galaxy assembly, with a tail out to $z > 6$ (Riechers et al. 2013). Previous works have shown that SMGs are extremely luminous in the infrared wavelengths ($L_{\text{IR}} \sim 10^{12} L_{\odot}$) with high star formation rates ($\text{SFR} \gtrsim 500 M_{\odot} \text{yr}^{-1}$; see e.g., reviews by Blain et al. 2002; Lagache et al. 2005; Casey et al. 2014). Following the pioneering works in the discovery of this population (Smail et al. 1997; Hughes et al. 1998; Barger et al. 1998), considerable amounts of effort have been invested into obtaining large samples of SMGs by carrying out large sky surveys with (sub)-mm facilities such as the *Herschel Space Observatory* (e.g., H-ATLAS, SPT, HERMES; Eales et al. 2010; Carlstrom et al. 2011; Oliver et al. 2012).

To characterize the physical properties of the gas reservoirs in the interstellar medium (ISM) where active star formation takes place, carbon monoxide (¹²CO) rotational lines have been commonly used as tracers due to its high abundance in the ISM as well as its low excitation energy; the ground state transition line thereby directly probes the cool gas that is essential to fuel star formation (see e.g., reviews by Solomon & Vanden Bout 2005; Carilli & Walter 2013). Observations of CO in SMGs have demonstrated that these galaxies have large gas reservoirs typical of $> 10^{10} M_{\odot}$ (e.g., Frayer et al. 1998; Neri et al. 2003; Riechers et al. 2011a,b; Ivison et al. 2011; Bothwell et al. 2013).

Many recent detailed studies have been carried out on

SMGs that are gravitationally lensed, as lensing amplifies the intrinsic fluxes of these sources, making them the brightest unveiled in large sky surveys (Negrello et al. 2010; Vieira et al. 2010; Oliver et al. 2012), and making follow-up studies considerably less time consuming. A particularly interesting and peculiar lensing system was discovered serendipitously in a study carried out with the *Herschel Space Observatory*, in which a type-2 quasar host SMG — SMM J0939+8315 (hereafter SMM J0939) is being lensed by the double-lobed Fanaroff-Riley Class II (FR-II; Fanaroff & Riley 1974) radio galaxy 3C220.3 at $z = 0.685$, which has a companion galaxy “B” as detected in Keck 2.2 μm and the *Hubble Space Telescope* 702nm images (Haas et al. 2014, hereafter H14). SMM J0939 is currently one of the brightest known lensed SMGs, with a lensing-magnified flux density of $S_{250\mu\text{m}} = 440 \pm 15$ mJy. Detections of C IV 1549Å and He II 1640Å line emission toward SMM J0939 place the redshift of this galaxy at $z = 2.221$. Based on the spectral line fluxes and line widths, H14 suggest the presence of an obscured active galactic nucleus (AGN) in the form of a type-2 quasar in this SMG.

In this paper, we present the detection of CO($J = 3 \rightarrow 2$) line emission toward the background SMG obtained with the Combined Array for Research in Millimeter Astronomy (CARMA), which confirms and refines the redshift, and permits a study of the physical conditions in the ISM of SMM J0939 in great detail. We report the detection of the continuum emission underlying the CO line and place constraints on the spectral energy distribution (SED) of the foreground FR-II galaxy at millimeter (mm) wavelengths (~ 104

GHz). Based on the magnification factor derived from our lens model, we infer various intrinsic properties of SMM J0939. We conclude this paper by comparing our findings to other similarly bright, strongly-lensed SMGs, as well as other type-2 quasars at $z \sim 2-3$.

We adopt a flat Λ CDM cosmological model throughout this paper, with $H_0 = 69.32 \text{ km Mpc}^{-1} \text{ s}^{-1}$, $\Omega_M = 0.286$, $\Omega_\Lambda = 0.713$, based on the WMAP9 results (Hinshaw et al. 2013). The luminosity distances at $z = 0.685$ and $z = 2.221$ are 4214 Mpc and 18052 Mpc, respectively; $1''$ corresponds to 7.169 kpc at $z = 0.685$, and 8.406 kpc at $z = 2.221$.

2. OBSERVATIONS

2.1. CARMA

Observations of the $\text{CO}(J=3 \rightarrow 2)$ rotational transition ($\nu_{\text{rest}} = 345.7959899 \text{ GHz}$) toward the background galaxy SMM J0939 ($z = 2.221$) were carried out using CARMA at a redshifted frequency of $\nu_{\text{obs}} = 107.357 \text{ GHz}$ (2.79 mm; program ID: cf0142; PI: Riechers). The 3 mm receivers were used to cover the redshifted $\text{CO}(J=3 \rightarrow 2)$ line and the nearby observed-frame 2.88 mm continuum emission. The correlator was configured to provide an effective bandwidth of 3.708 GHz in each sideband, and a spectral resolution of 5.208 MHz ($\sim 14.5 \text{ km s}^{-1}$). The line was placed in the upper sideband, with the local oscillator tuned to $\nu_{\text{LO}} \sim 104.2609 \text{ GHz}$. Observations were carried out under good weather conditions in the E array configuration on 2014 July 12. This resulted in 1.56 hours of 15 antenna-equivalent on-source time after discarding unusable visibility data. The nearby source J1039+811 (0.65 Jy) was observed every 20 minutes for pointing, amplitude, and phase calibration. Mars was observed as the primary absolute flux calibrator, and the quasar 3C273 was observed as the secondary flux calibrator. J0927+390 was observed for bandpass calibration, yielding $\sim 15\%$ calibration accuracy.

We use the MIRIAD package to calibrate and analyze the visibility data, which are deconvolved and imaged with “natural” weighting. This yields a synthesized clean beam size of $11''.5 \times 6''.2$, -56.1° east of north for the upper sideband image cube and an rms noise of $\sigma_{\text{ch}} = 9.49 \text{ mJy beam}^{-1}$ per channel of width $\sim 29 \text{ km s}^{-1}$. The continuum image is created by averaging over all line-free channels; this yields a synthesized clean beam of $12''.0 \times 6''.5$, -55.9° east of north, and an rms noise of $\sigma_{\text{cont}} = 0.50 \text{ mJy beam}^{-1}$ over 6.8 GHz.

3. RESULTS

3.1. Foreground Galaxy: 3C220.3

Averaging over all line-free channels, we detect continuum emission at $\sim 9\sigma$ significance at an averaged frequency of $\nu_{\text{cont}} = 104.2106 \text{ GHz}$ ($\sim 2.9 \text{ mm}$) in the observed-frame, corresponding to 175.6 GHz ($\sim 1.7 \text{ mm}$) at $z = 0.685$. In this lensing system, the foreground galaxy (3C220.3) is radio-loud, we thus expect it to be the dominant contributor to the continuum emission (see §4.2.1 for details). The task IMFIT is used to estimate the peak position of the continuum emission, where the flux density is $S_\nu = 4.93 \pm 0.31 \text{ mJy beam}^{-1}$. From the continuum measurement, the deconvolved source size is $(8''.4 \pm 1''.1) \times (4''.9 \pm 0''.6)$ at -53.8° , and the integrated

flux density is $7.39 \pm 1.42 \text{ mJy}$. An overlay image of the 104 GHz continuum emission with the 9 GHz continuum emission (H14) is shown in Figure 1, demonstrating that the continuum emission is marginally resolved at the resolution of our observations. It is therefore plausible that non-thermal emission from the radio lobes and core of the foreground galaxy dominate the integrated flux density of the measured continuum. We discuss this further in Section 4.2.1.

The frequency range of our observations covers the $\text{HCO}^+(J=2 \rightarrow 1)$, $\text{HNC}(J=2 \rightarrow 1)$, and $\text{H}_2\text{O}(3_{13} \rightarrow 2_{20})$ transition lines in the foreground galaxy, at the redshifted frequencies of 105.86, 107.71, and 108.79 GHz, respectively. We establish 3σ upper limits employing a typical FWHM line width of $\sim 300 \text{ km s}^{-1}$, based on the $\text{CO}(J=1 \rightarrow 0)$ line measurements in a sample of local radio galaxies ($z < 0.1$; Smolčić & Riechers 2011). This results in upper limits of $< 2.66 \text{ Jy km s}^{-1}$ on the integrated emission line strengths.

3.2. Background Galaxy: SMM J0939

We detect $\text{CO}(J=3 \rightarrow 2)$ line emission at $\sim 8\sigma$ significance toward the background SMG SMM J0939 at $z = 2.221$. The lensing-magnified spatial extent of this SMG is $\sim 5''$, as shown in the Submillimeter Array (SMA) 1 mm dust continuum image in Figure 2 (H14); as such, the detected $\text{CO}(J=3 \rightarrow 2)$ line emission is spatially unresolved. We therefore extract the line profile (Figure 2) at the peak position of the unresolved CO emission. Fitting a four-parameter single Gaussian to the spectrum yields a peak flux density of $21.61 \pm 2.66 \text{ mJy}$, superimposed on a continuum level of $4.15 \pm 0.48 \text{ mJy beam}^{-1}$, and a line full width at half-maximum (FWHM) of $546 \pm 36 \text{ km s}^{-1}$.

We construct a velocity-integrated (0th moment) map of the $\text{CO}(J=3 \rightarrow 2)$ line emission after subtracting continuum emission in the visibility plane. This results in a velocity-integrated $\text{CO}(J=3 \rightarrow 2)$ line flux of $I_{\text{CO}} = 12.6 \pm 2.0 \text{ Jy km s}^{-1}$ over a velocity range of $\Delta v \sim 1420 \text{ km s}^{-1}$, the uncertainty does not include $\sim 15\%$ calibration uncertainty. Our $\text{CO}(J=3 \rightarrow 2)$ line measurement confirms the redshift of SMM J0939, yielding $z = 2.2212 \pm 0.0010$.

4. ANALYSIS

4.1. Lens Modelling

To study the intrinsic properties of the background galaxy, we determine the magnification factor and the half-light radius of the dust region by performing lens modeling on the SMA 1 mm continuum data presented by H14 of this system. Lens modeling is carried out in the visibility (uv -) plane using an updated version of the publicly available software UVMCMCFIT (Bussmann et al. 2015a), details of the parametric lens model can be found in Bussmann et al. (2015b). The surface mass densities of the two lensing galaxies, 3C220.3 and its companion galaxy B, are described by singular isothermal ellipsoid profiles, and the source is assumed to have an elliptical Gaussian profile.

The resulting best-fit model as shown in Figure 3 shows no significant bowls in the residual image, and the knots (lensed emission) in the observed SMA data

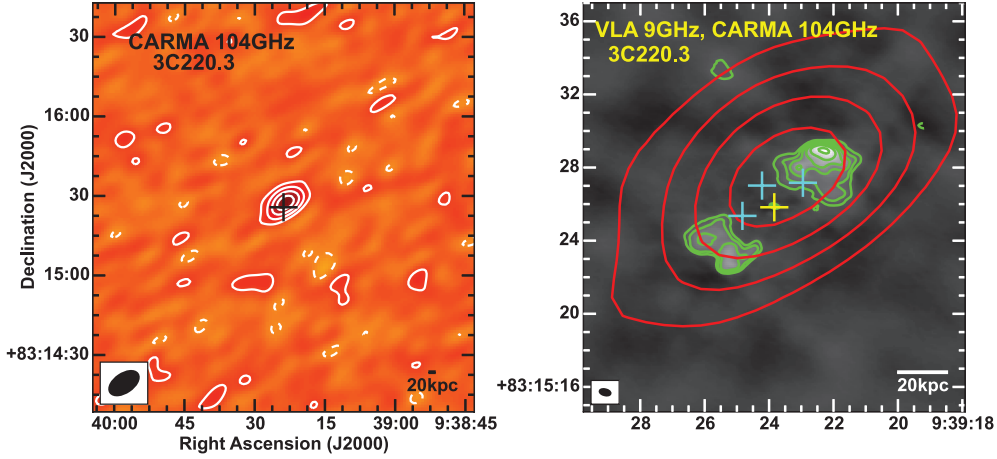


Figure 1. Left: Contour map of the 104 GHz continuum emission in the foreground radio galaxy 3C220.3. The beam size is $12''.0 \times 6''.5$, at P.A. = -56° , as indicated in the bottom left corner. Right: CARMA 104 GHz continuum emission (red contours) overlaid on the VLA 9 GHz continuum emission (green contours and grayscale; H14). The synthesized beam size of the VLA observations is $0''.6 \times 0''.2$, at P.A. 76° . The contour levels of the 104 GHz continuum emission start at $\pm 2\sigma$, incrementing at steps of $\pm 2\sigma$, where $\sigma = 0.5 \text{ mJy beam}^{-1}$. The contour levels of the 9 GHz continuum emission start at $\pm 4\sigma$, where $\sigma = 0.064 \text{ mJy beam}^{-1}$, and increment at steps of $\pm 2^n \sigma$, where n is a positive integer. The blue crosses correspond to the centroid locations of the lensing knots detected in the SMA 1 mm continuum emission (see Figure 2). The central cross on each panel indicates the position of the radio core of 3C220.3.

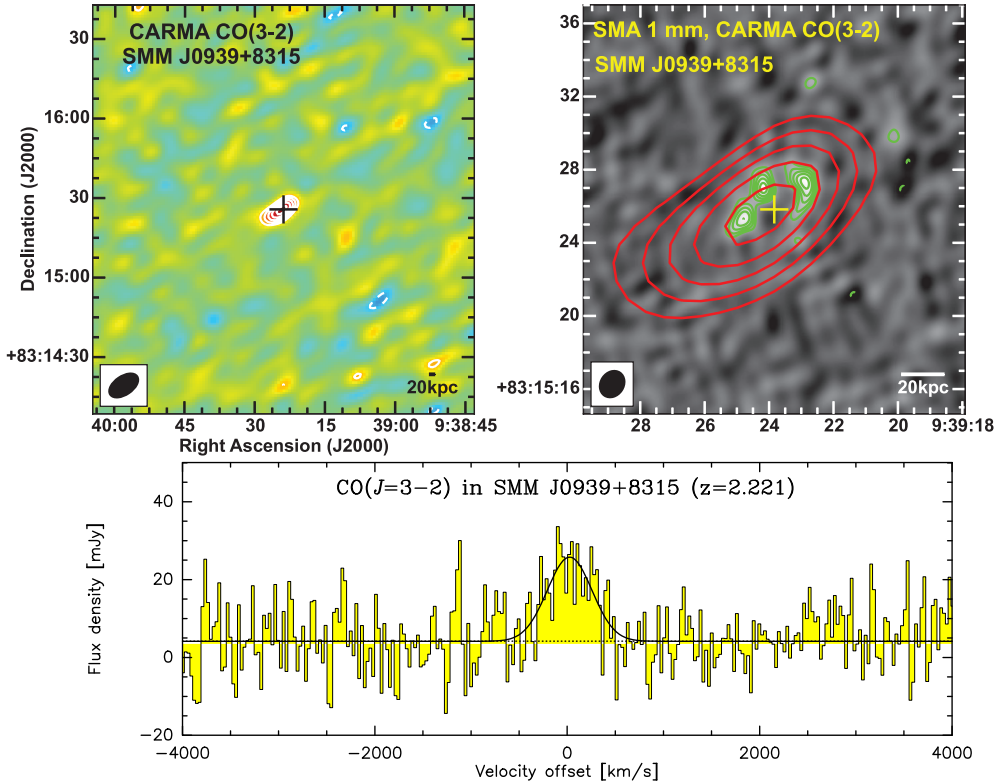


Figure 2. Top Left: Continuum-subtracted moment-0 map of $\text{CO}(J=3 \rightarrow 2)$ line emission toward the background SMG with $\sigma = 1.03 \text{ Jy km s}^{-1} \text{ beam}^{-1}$ over a velocity range of $\Delta v \sim 514 \text{ km s}^{-1}$. The beam size is $11''.5 \times 6''.2$, at P.A. = -56° , as indicated in the bottom left corner. Top Right: Velocity-integrated $\text{CO}(J=3 \rightarrow 2)$ line emission (red contours) overlaid on the SMA 1 mm dust continuum (green contours and grayscale; H14), with an rms noise of $\sigma_{1 \text{ mm}} = 0.84 \text{ mJy beam}^{-1}$. The beam size of the SMA observations is $1''.4 \times 1''.2$, P.A. -34° , as shown in the bottom left corner. The central cross on each image corresponds to the same coordinates as in Figure 1. The contour levels in both images start at $\pm 3\sigma$, incrementing at steps of $\pm 1\sigma$. Bottom: Spectrum extracted at the peak position of CO line emission, with a spectral resolution of $\Delta v \sim 29 \text{ km s}^{-1}$, and an rms of $\sigma_{\text{ch}} = 9.5 \text{ mJy beam}^{-1}$ per channel. The solid black line shows a Gaussian fit to the $\text{CO}(J=3 \rightarrow 2)$ line profile, where the velocity scale is relative to $z = 2.221$.

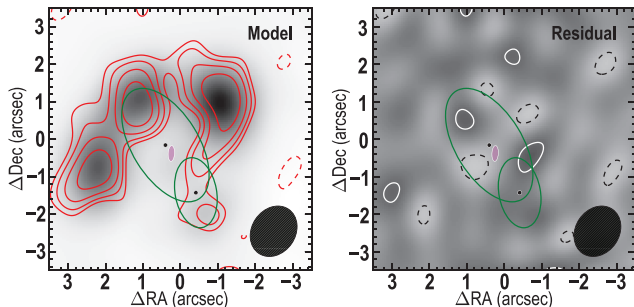


Figure 3. Double-lens modeling of SMM J0939 using UVMCMCFIT on the SMA 1 mm continuum data. The contours start at $\pm 2\sigma$, incrementing at steps of $\pm 2\sqrt{2}\sigma$ in both panels. Left: SMA 1 mm continuum (red contours) overlaid on the best-fit model (grayscale image), assuming an elliptical Gaussian profile for the background SMG. The lenses are represented by the black dots, the half-light area of the background source is represented by the magenta ellipse, and the critical curves are represented by the green ellipses. Right: Residual contours and image obtained by taking the Fourier transform of the difference between the SMA data and the best-fit model in the visibility plane. Solid (dashed) contours show the positive (negative) residuals.

Table 1
Lens modeling parameters and results

Parameters		Best-Fit Values	
Lens 0 (3C220.3)			
Offset in RA	$\Delta\alpha_{\text{lens}0}$ (")		0.403 ± 0.026
Offset in Dec	$\Delta\delta_{\text{lens}0}$ (")		-0.181 ± 0.027
Axial Ratio	$q_{\text{lens}0}$		0.446 ± 0.063
Position angle	$\phi_{\text{lens}0}$ (deg)		31.56 ± 4.15
Einstein radius	θ_{E0} (")		1.218 ± 0.010
Lens 1 (Companion galaxy B)			
Offset in RA	$\Delta\alpha_{\text{lens}1}$ (")		-0.804 ± 0.034
Offset in Dec	$\Delta\delta_{\text{lens}1}$ (")		-1.243 ± 0.017
Axial ratio	$q_{\text{lens}1}$		0.608 ± 0.138
Position angle	$\phi_{\text{lens}1}$ (deg)		14.2 ± 15.7
Einstein radius	θ_{E1} (")		0.745 ± 0.015
Source (SMM J0939)			
Offset in RA	$\Delta\alpha_s$ (")		-0.163 ± 0.035
Offset in Dec	$\Delta\delta_s$ (")		-0.193 ± 0.048
Axial ratio	q_s		0.424 ± 0.237
Position angle	ϕ_s (deg)		174.34 ± 8.89
Effective radius	r_s (")		0.106 ± 0.033
Magnification factor	μ_L		10.13 ± 1.38

Note. — All angular offsets are with respect to $\alpha = 9^{\text{h}}39^{\text{m}}23^{\text{s}}.54$, $\delta = 83^{\circ}15'26''10$ (J2000). The corresponding masses within the Einstein radii of the galaxies 3C220.3 and its companion galaxy B are $M(\theta < \theta_E) = (4.86 \pm 0.08) \times 10^{11} M_{\odot}$ and $M(\theta < \theta_E) = (1.82 \pm 0.07) \times 10^{11} M_{\odot}$, respectively.

are reproduced well by the best-fit model. Our best-fit model yields a magnification factor of $\mu_L = 10.13 \pm 1.38$ and a half-light radius of $r_s = 0''.11 \pm 0''.03$, corresponding to ~ 0.9 kpc at $z = 2.221$. All best-fit parameters are listed in Table 1.

4.2. SED Fitting

4.2.1. 3C220.3

Synchrotron continuum emission from extended components of a radio galaxy decreases with increasing radio frequencies, and the spectrum is commonly characterized by a power law distribution $S \propto \nu^{-\alpha}$, where the

spectral index α is $\gtrsim 0.5$. While the contribution from extended components decreases, studies using samples of radio galaxies have suggested that the flat/inverted-spectrum of the compact radio core component rises and dominates the flux density at higher frequencies (Kellermann & Pauliny-Toth 1981; Begelman et al. 1984). This has been observed in a FR-II galaxy at similar redshift — 3C220.1 at $z = 0.610$, where observations were carried out at the observed-frame frequency of ~ 90 GHz (Hardcastle & Looney 2008).

Previously, an upper limit of < 0.17 mJy at 4.6 GHz has been established by Mullin et al. (2006) on the core component of 3C220.3, and an unambiguous detection of 0.8 mJy at 9 GHz has been reported by H14, suggesting a substantially inverted spectrum of the core (Figure 4). Consequently, we may naively expect the integrated flux density in our continuum detection of $S_{104\text{GHz}} = 7.39 \pm 1.42$ mJy to be dominated by the unresolved core component of the foreground FR-II galaxy, which is at $z = 0.685$. However, the deconvolved spatial size of the source matching that in the resolved image (see Figure 1) is suggestive of a marginally resolved detection of the extended lobe components. This is plausible given that the orientation of the synthesized beam in our observations is in alignment with the axis along the lobes of the radio galaxy, as shown in Figure 1. We investigate this disparity by fitting models to existing SED measurements as listed in Table 2, and extrapolating the fit to estimate the flux density of the lobes at the frequency of our continuum measurement.

Following Equation (1) in Cleary et al. (2007), the fit to the lobe emission can be expressed as a parabolic function:

$$\log F_{\nu}^{\text{lobe}}(\nu) \propto -\beta (\log \nu - \log \nu_t)^2 + \log(\exp(\frac{\nu}{\nu_c^{\text{lobe}}})) \quad (1)$$

where F_{ν}^{lobe} is the flux density of the lobes, β is a parameter representing the bending of the parabola, ν_t is the frequency at which the optical depth of the synchrotron emitting plasma reaches unity, and ν_c^{lobe} is the frequency corresponding to the cutoff energy of the lobe plasma energy distribution. The extrapolated flux density at 104 GHz is consistent with the peak flux density of our continuum measurement (Figure 4). The 9σ detection of the continuum thereby suggests a dominant contribution from the lobes, and that the peak flux density is not dominated by emission toward the core. Moreover, the peak position of the 104 GHz continuum is centered toward the brighter northern lobe (Figure 1), which further supports our argument. Consequently, a conservative upper limit of $S_{\nu} < 4.93$ mJy on the core emission can be established using the measured peak flux density. Yet, by considering the difference between the integrated flux density from our measurement and the flux density from an extrapolation of the model (see Figure 4; $S_{104\text{GHz, fit}} = 5.10$ mJy), we establish a more stringent constrain on this upper limit of $S_{\nu} < 2.29$ mJy. We did not extrapolate the core measurements to the frequency of our continuum, as previous measurements of the core are taken across different epochs, and the core may be time-variable.

Studies by Meisenheimer et al. (1989) and Hardcastle & Looney (2008) have suggested that spectra of hotspots are flat up to optical frequencies, where some

Table 2
Continuum data of the lensing galaxy 3C220.3 and background SMG SMM J0939

Wavelength	Flux Density	Instrument
SMM J0939		
70 μm	29.5 ± 5 mJy	PACS
100 μm	102 ± 7 mJy	PACS
160 μm	289 ± 9 mJy	PACS
250 μm	440 ± 15 mJy	SPIRE
350 μm	403 ± 20 mJy	SPIRE
500 μm	268 ± 30 mJy	SPIRE
1000 μm	$51 \pm 14^{\text{a}}$ mJy	SMA
Frequency	Flux Density	Reference
3C220.3 Integrated (Core & Lobes)		
104.2 GHz	$7.39 \pm 1.42^{\text{b}}$ mJy	LR16
10.7 GHz	270 ± 30 mJy	KP73
10.7 GHz	253 ± 28 mJy	L80
5.0 GHz	640 ± 100 mJy	K69
5.0 GHz	636 ± 50 mJy	L80
2.7 GHz	1.33 ± 0.07 Jy	K69
2.7 GHz	1.34 ± 0.10 Jy	L80
1.4 GHz	2.95 ± 0.09 Jy	C98
1.4 GHz	2.99 ± 0.06 Jy	P66
1.4 GHz	2.80 ± 0.14 Jy	K69
1.4 GHz	2.89 ± 0.09 Jy	L80
0.75 GHz	5.94 ± 0.28 Jy	L80
0.75 GHz	5.94 ± 0.21 Jy	P66
0.75 GHz	5.60 ± 0.84 Jy	K69
352 MHz	11.3 ± 0.453 Jy	WENSS
352 MHz	11.6 ± 0.464 Jy	WENSS
178 MHz	15.7 ± 2.35 Jy	K69
178 MHz	17.1 ± 1.71 Jy	L80
152 MHz	22.6 ± 0.08 Jy	B85
152 MHz	22.5 ± 0.04 Jy	B85
86 MHz	51.6 ± 9.90 Jy	L80
73.8 MHz	37.5 ± 3.82 Jy	C07
38 MHz	49.6 ± 4.96 Jy	L80
38 MHz	40.2 ± 6.30 Jy	K69
37.8 MHz	60.7 ± 6.07 Jy	H95
17.8 MHz	64.9 ± 6.49 Jy	H95
3C220.3 (Core Only)		
104.2 GHz	$< 2.29^{\text{c}}$ mJy	LR16
9.0 GHz	0.80 ± 0.06 mJy	H14
4.86 GHz	< 0.17 mJy	M06

References. — B85 = Baldwin et al. (1985); C98 = Condon et al. (1998); C07 = Cohen et al. (2007); H95 = Hales et al. (1995); H14 = Haas et al. (2014); K69 = Kellermann et al. (1969); KP73 = Kellermann & Pauliny-Toth (1973); L80 = Laing & Peacock (1980); LR16 = this work; M06 = Mullin et al. (2006); P66 = Pauliny-Toth et al. (1966); WENSS = Rengelink et al. (1997)[†]

Note. — Photometric data of SMM J0939 are from Haas et al. (2014).

^a Errors include calibration uncertainties

^b Integrated flux density. Peak flux density of the continuum emission is 4.93 ± 0.31 mJy beam⁻¹

^c Constraint from SED modeling

[†] www.astron.nl/wow/testcode.php?survey=1

exhibit spectral steepening in cm and mm wavelengths (e.g., 3C123). At the resolution of our observations, it remains unclear whether the measured flux density is dominated by emission from the compact hotspots or that from the surrounding diffuse lobe components.

4.2.2. SMM J0939+8315

To constrain the dust and gas properties in the ISM of SMM J0939, we perform SED fitting to the photo-

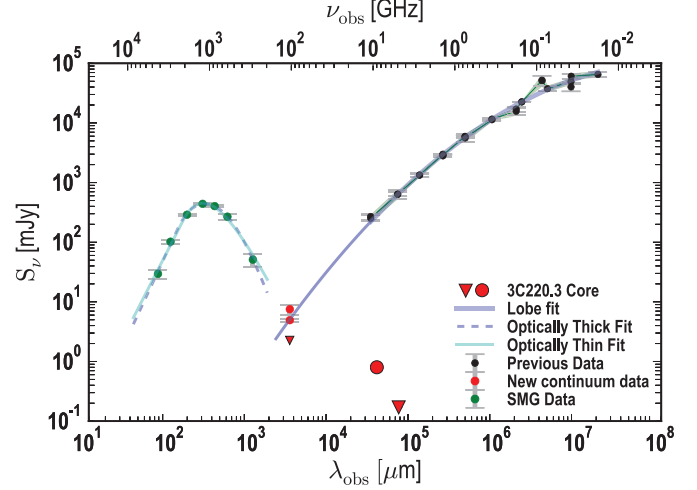


Figure 4. SEDs of 3C220.3 (solid purple line) and SMM J0939 (dashed purple line and solid cyan line) including the new measurements presented in this paper. The solid purple line corresponds to the parabolic function we fit to the existing data associated with 3C220.3 (black dots; see Table 2). The red dots at 104 GHz correspond to our continuum measurements (integrated and peak, respectively), and the red triangles correspond to the upper limits on the radio core. The dashed purple line and the solid cyan line correspond to the best-fit optically thick and optically thin models of SMM J0939, respectively, using the photometric data from H14.

metric data obtained with *Herschel*/PACS and SPIRE, at wavelengths between observed-frame $70 \mu\text{m} - 500 \mu\text{m}$, and the interferometric data obtained with the SMA at 1 mm (H14). We use the publicly available software MBB_EMCEE¹ to perform the SED fitting; the code uses an affine-invariant Markov chain Monte Carlo (MCMC) approach, and further details of the code are given by Riechers et al. (2013) and Dowell et al. (2014).

The functional form of the fit comprises a single-temperature, modified blackbody function joined to a $B_\lambda \propto \lambda^\alpha$ power law on the blue side of the SED. We fit both optically thick and optically thin models. In the optically thick case, the wavelength $\lambda_0 = c/\nu_0$ is an additional parameter representing the rest-frame wavelength at which the optical depth $\tau_\nu = (\nu/\nu_0)^\beta$ reaches unity. Thus, the functional form of the modified blackbody in the optically thick regime is as follows:

$$B_\lambda \propto \frac{(1 - \exp(-\frac{\lambda_0(1+z)}{\lambda})^\beta) (\frac{c}{\lambda})^3}{\exp^{\frac{hc}{\lambda kT/(1+z)}} - 1} \quad (2)$$

and in the optically thin regime, the functional form reduces to:

$$B_\lambda \propto \frac{(\frac{c}{\lambda})^{\beta+3}}{\exp^{\frac{hc}{\lambda kT/(1+z)}} - 1} \quad (3)$$

where T is the rest-frame cold dust temperature, β is the dust emissivity index, and α is the mid-infrared power law spectral index. The overall fit is normalized using the observed-frame $500 \mu\text{m}$ flux density, hence this becomes an additional parameter ($f_{\text{norm}, 500\mu\text{m}}$) in the fit. For both models, we impose an upper limit of 60 K on the observed-frame dust temperature ($T/(1+z)$), and an

¹ https://github.com/aconley/mbb_emcee

Table 3
SED fitting results

Parameters	Optically Thick	Optically Thin
χ^2	2.25	5.31
D.O.F	2	3
T (K)	$63.1^{+1.1}_{-1.3}$	$52.0^{+1.3}_{-1.2}$
β	$1.9^{+0.6}_{-0.5}$	$0.7^{+0.2}_{-0.3}$
α	$2.9^{+0.3}_{-0.4}$	$2.8^{+0.2}_{-0.2}$
λ_0^a (μm)	$248.7^{+86.0}_{-123.8}$	—
λ_{peak}^b (μm)	$254.7^{+6.2}_{-6.1}$	$301.4^{+29.0}_{-30.1}$
$f_{\text{norm}, 500\mu\text{m}}^c$ (mJy)	$267.4^{+16.7}_{-16.3}$	$244.3^{+15.3}_{-15.3}$
L_{IR}^d ($10^{12} L_{\odot}$)	$88.5^{+2.6}_{-2.6}$	$89.2^{+2.5}_{-2.5}$
M_{dust}^e ($10^8 M_{\odot}$)	$50.5^{+20.4}_{-20.2}$	$25.7^{+3.9}_{-5.5}$

Note. — Errors reported here are $\pm 1\sigma$. L_{IR} and M_{d} are reported prior to lensing correction.

^a Rest-frame wavelength where $\tau_{\nu} = 1$

^b Observed-frame wavelength of the SED peak

^c Observed-frame flux density at $500 \mu\text{m}$

^d Rest-frame 8–1000 μm luminosity

^e Derived assuming a standard absorption mass coefficient $\kappa = 2.64 \text{ m}^2 \text{ kg}^{-1}$ at $\lambda = 125.0 \mu\text{m}$ (Dunne et al. 2003)

upper limit of 2.2 on β . For the optically thick model, we impose an additional upper limit of $3000 \mu\text{m}$ on $\lambda_0(1+z)$.

The best-fit values in both regimes are listed in Table 3, and the correlation plots are available in the Appendix. The best-fit solution of optically thin models corresponds to $\chi^2 = 5.31$ with 3 degrees of freedom, whereas that of optically thick models corresponds to $\chi^2 = 2.25$ with 2 degrees of freedom, suggesting a better fit than in the optically thin case. In the subsequent analysis, we employ the inferred values from the optically thick model. The best-fit solution yields a far-infrared luminosity (rest-frame $42.5\text{--}122.5 \mu\text{m}$) of $L_{\text{FIR}} = 53.3^{+1.1}_{-1.1} \times 10^{12} L_{\odot}$, and a total infrared (IR; rest-frame 8–1000 μm) luminosity of $L_{\text{IR}} = 88.5^{+2.6}_{-2.6} \times 10^{12} L_{\odot}$ ². Assuming a dust absorption coefficient of $\kappa_{\nu} = 2.64 \text{ m}^2 \text{ kg}^{-1}$ at $125.0 \mu\text{m}$ (Dunne et al. 2003), we find a dust mass of $M_{\text{dust}} = 50.5^{+20.4}_{-20.2} \times 10^8 M_{\odot}$; the uncertainties do not include those in the dust absorption coefficient (κ_{ν}). These properties are derived based on the SED fitting to the photometric data, *i.e.*, prior to lensing correction. We note that the dust mass is weakly constrained owing to the dearth of data in the rest-frame FIR waveband. As such, we investigate how the dust mass would be affected by fitting additional optically thick models with an upper limit of β adjusted from 2.2 to 3.0. While the difference in each best-fit parameter between this scenario and the previous models (with an upper limit of $\beta = 2.2$) is within 3%, we find that the dust mass inferred from this best-fit SED model is boosted by a factor of ~ 2 .

4.3. Physical Properties of the ISM in SMM J0939

4.3.1. Molecular Gas Mass

While the ground state CO transition line traces the cold molecular gas in the ISM (*e.g.*, Wilson, Jefferts, &

² Owing to the positive K-correction blue-ward of the dust peak, in which the foreground radio galaxy contributes a non-negligible amount to the MIR luminosity, we do not fit for a separate AGN component. Instead, we adopt a power-law to account for the MIR excess, which allows us to estimate the IR luminosity (*e.g.*, Casey 2012; Riechers et al. 2013; Kirkpatrick et al. 2015).

Penzias 1970; Downes & Solomon 1998), transition lines of higher rotational states ($J > 1$) are frequently observed in high-redshift sources as the ground state transition line is redshifted to lower frequencies that can only be observed with traditional radio telescopes (Carilli & Walter 2013). Consequently, assumptions on the CO excitation conditions are required to derive the molecular gas mass using the $M(\text{H}_2)$ -to- L'_{CO} conversion factor (α_{CO}) when extrapolating from higher- J CO lines.

Recent observations in high-redshift quasar hosts suggest that the ratio is $R_{31} \sim 1$ (Riechers et al. 2006, 2011c). In the case of high-redshift type-2 quasars, Riechers et al. (2011c) report a brightness temperature ratio of $R_{31} = 1.00 \pm 0.10$ for IRAS F10214+4724 (hereafter F10214), which is currently the only known type-2 quasar with both $\text{CO}(J=3 \rightarrow 2)$ and $\text{CO}(J=1 \rightarrow 0)$ line measurements. Here, we derive the molecular gas mass assuming thermalized excitation of CO, as SMM J0939 is postulated to be hosting a type-2 quasar (H14).

We calculate the $\text{CO}(J=1 \rightarrow 0)$ line luminosity using a standard relation (*e.g.*, Solomon & Vanden Bout 2005) and assuming a conversion factor of $\alpha_{\text{CO}} = 0.8 M_{\odot} (\text{K km s}^{-1} \text{ pc}^2)^{-1}$ based on empirical relations from local ULIRGs, which is typically adopted for SMGs (*e.g.*, Tacconi et al. 2006, 2008; Bothwell et al. 2013). This corresponds to $L'_{\text{CO}(1-0)} = (3.42 \pm 0.71) \times 10^{10} (10.1/\mu_{\text{L}}) \text{ K km s}^{-1} \text{ pc}^2$; hence the inferred total molecular gas mass is $M_{\text{gas}} = (2.74 \pm 0.57) \times 10^{10} M_{\odot}$ after correcting for lensing magnification. This results in a gas-to-dust ratio of $f_{\text{gas-dust}} = M_{\text{gas}}/M_{\text{dust}} = 55 \pm 24$. This is in good agreement with the values found for other SMGs (Coppin et al. 2008; Michałowski et al. 2010; Riechers et al. 2011a).

4.3.2. Star Formation Rate & Star Formation Efficiency

We derive the SFR using the lensing-corrected far-infrared luminosity assuming that the dominant heating source of cold-dust is young and massive stars, and that a contribution from the dust-enshrouded AGN is negligible. This assumption stems from the results of recent studies using various approaches, such as spectral decomposition techniques and correlation between far-infrared luminosity and other tracers of star-formation, suggesting that far-infrared emission dominantly originates from star-formation in host galaxies, even in the most energetic QSOs (*e.g.*, Netzer et al. 2007; Mullaney et al. 2011; Harrison et al. 2015).

Using the Kennicutt (1998) relation and adopting a Chabrier (2003) stellar initial mass (IMF) function, we find a $\text{SFR}_{\text{FIR}} = 526 \pm 73 M_{\odot} \text{ yr}^{-1}$. The starburst in SMM J0939 can be maintained at its current rate for a time that can be approximated by the gas depletion timescale, $\tau_{\text{depl}} = M_{\text{gas}}/\text{SFR}$, which assumes no replenishment of gas and feedbacks. This corresponds to $\tau_{\text{depl}} = 52 \pm 8 \text{ Myr}$, which is in good agreement with those found in other SMGs (*e.g.*, Greve et al. 2005).

The SFR per unit mass of molecular gas is commonly taken as a measure of the star formation efficiency. We compute this ratio using the far-infrared and CO luminosities. The derived SFE is therefore independent of the magnification factor, the CO luminosity to gas mass conversion factor (α_{CO}), and the IMF. This, however, assumes that differential lensing between the CO and

far-infrared emission is negligible. The resulting ratio is $\text{SFE}_{\text{FIR}} = 154 \pm 25 L_{\odot} (\text{K km s}^{-1} \text{pc}^2)^{-1}$, this is comparable to those found in “typical” SMGs (Greve et al. 2005; Tacconi et al. 2006; Riechers et al. 2011a).

We compute the surface densities by dividing half the SFR and gas mass by the area subtended by the half-light radius (e.g., Genzel et al. 2010; Harrison et al. 2015), yielding $\Sigma_{\text{SF}} = 106 M_{\odot} \text{ yr}^{-1} \text{ kpc}^{-2}$ and $\Sigma_{\text{gas}} = 5.48 \times 10^9 M_{\odot} \text{ kpc}^{-2}$, respectively. These results are in good agreement with values typical for SMGs (Tacconi et al. 2006; Hodge et al. 2015). The inferred surface densities of SMM J0939 follow a universal Schmidt-Kennicutt relation between the star formation rate surface density and the molecular gas surface density: $\Sigma_{\text{SF}} = 9.3 (\pm 2) \times 10^{-5} (M_{\text{gas}}/2\pi R_{1/2}^2)^{1.71 (\pm 0.05)}$, which was derived using a sample consisting of local star-forming galaxies and high-redshift galaxies out to $z \sim 2.5$, and assuming a Chabrier IMF (Bouché et al. 2007).

4.3.3. Physical Size and Dynamical Mass

Our lens model suggests a half-light radius of $r_s \sim 1 \text{ kpc}$ for the dust-emitting region in SMM J0939. This is comparable to the half-light radii found in other SMGs with high resolution imaging. Similar sizes have been reported by Bussmann et al. (2013), who find typical radii of 1.5 kpc for a sample of *Herschel*-selected lensed SMGs with $S_{500\mu\text{m}} > 100 \text{ mJy}$. Also, Simpson et al. (2015) report a radial extent of 1.2 kpc for a sample of un-lensed SMGs with $S_{850\mu\text{m}} = 8\text{--}16 \text{ mJy}$.

We estimate the dynamical mass of SMM J0939 using our $\text{CO}(J=3 \rightarrow 2)$ line measurement and assuming that the molecular gas is virialized. With this assumption, we use an isotropic virial estimator (e.g., Engel et al. 2010), with the FWHM of the $\text{CO}(J=3 \rightarrow 2)$ line profile and the half-light radius from our lens model for R_{eff} , assuming that the dust emission traces the same emitting region as the CO. We find a dynamical mass of $M_{\text{dyn}} = (7.84 \pm 2.84) \times 10^{10} M_{\odot}$, and a gas-to-dynamical mass fraction of $f_{\text{gas-to-dyn}} = 0.35 \pm 0.14$, consistent with those of other SMGs (Tacconi et al. 2006). We note that a derived dynamical mass based on this assumption is likely to be biased towards low values, as the CO-emitting region can be apparently more extended than the dust emitting region due to the low dust optical depth at larger radii. This is supported by recent studies, in which CO source sizes ranging from $\sim 4\text{--}20 \text{ kpc}$ have been found, which are larger than typical dust continuum sizes (Tacconi et al. 2006; Riechers et al. 2011a; Ivison et al. 2011; Hodge et al. 2013, 2015).

5. DISCUSSION AND CONCLUSIONS

We present the detection of $\text{CO}(J=3 \rightarrow 2)$ line emission toward SMM J0939+8315, a strongly-lensed SMG that is hosting a type-2 quasar, refining the redshift to $z = 2.2212 \pm 0.0010$. The underlying continuum is detected at $\sim 9\sigma$ significance, where the flux density is likely dominated by emission from the lobes and hotspots of the foreground radio galaxy 3C220.3.

The detection of CO in SMM J0939 implies a CO luminosity of $L'_{\text{CO}(1-0)} = (3.4 \pm 0.7) \times 10^{10} (10.1/\mu_{\text{L}}) \text{ K km s}^{-1} \text{ pc}^2$, corresponding to a gas mass of $M_{\text{gas}} = (2.7 \pm 0.6 \times 10^{10} (10.1/\mu_{\text{L}}) M_{\odot})$. This suggests the presence of a massive molecular gas reservoir that fuels

the star formation activity taking place at a rate of $\sim 526 M_{\odot} \text{ yr}^{-1}$. If the star forming activity continues at the current rate, the gas reservoir will be depleted within $\lesssim 52 \text{ Myr}$, which is consistent with the short timescales found in other SMGs (Greve et al. 2005). The derived intrinsic properties of SMM J0939 are evident of ongoing rapid star formation; this is in good agreement with the current conjecture that SMGs are a population of high-redshift galaxies that build up the bulk of stellar mass in present-day galaxies, thus play an important role in galaxy formation and evolution (e.g., Dickinson et al. 2003).

We compare our findings for SMM J0939 with a sample of typically unlensed or only weakly magnified, $850 \mu\text{m}$ -selected SMGs (Bothwell et al. 2013, hereafter B13). Their properties are listed in Table 4, showing that SMM J0939 has properties similar to other SMGs studied to date. The gas mass in SMM J0939 is slightly lower than the median in the B13 sample, but we cannot rule out the possibility that this difference is due to the different assumptions made for the gas excitation conditions. The gas properties (CO luminosity and gas mass) of the SMGs in the B13 sample are derived based on the assumption of typical excitation conditions found from CO spectral line energy distribution (SLED) modelling of the sample average, which the authors find to be very similar to those of the cosmic Eyelash. Thus, we additionally compare SMM J0939 in more detail to two other well-studied, strongly-lensed SMGs with comparably high apparent submillimeter fluxes found at similar redshifts — HLSW-01 and the cosmic Eyelash. The properties of these sources are derived using similar approaches to those employed in this paper.

As shown in Table 4, while the cosmic Eyelash has the least amount of molecular gas, as well as the longest gas depletion timescale, the overall gas and dust properties of SMM J0939 fall between those of HLSW-01 and the cosmic Eyelash. Such distinction is likely a result of our selection bias: while these sources appear similarly bright at $250 \mu\text{m}$, the lensing magnification varies by a factor of ~ 3 . In particular, with the cosmic Eyelash having the highest lensing magnification among the three, this intrinsically fainter, and less gas-rich SMG appears notably bright at $250 \mu\text{m}$, while its CO line and IR luminosities are lower than those of most SMGs studied to date. While lensing can probe sources of various intrinsic properties, we find that SMM J0939 is consistent with the “typical” SMG population, with its intrinsic CO line luminosity, IR luminosity, dust mass, SFR, SFE, depletion timescale, and gas mass fraction comparable to those found in “typical” SMGs studied to date.

Since SMM J0939 also hosts a type-2 quasar, we compare its properties against those of eight CO-detected obscured AGNs at $z = 1.6\text{--}2.8$ (Polletta et al. 2011, and references therein). Among these obscured quasars, F10214 has the lowest molecular gas mass as well as SFR. The fact that the gas mass of F10214 in their compilation was derived using $\text{CO}(J=3 \rightarrow 2)$ line emission (Solomon & Vanden Bout 2005) has a minor effect on the resulting low gas mass; Riechers et al. (2011c) report a similarly low gas mass derived using their $\text{CO}(J=1 \rightarrow 0)$ line emission. With F10214 being the most strongly-lensed high-redshift type-2 quasar ($\mu_{\text{L}} = 17$; Solomon

& Vanden Bout 2005)³, its exceptionally low molecular gas mass and SFR is evident that this source lies on the low end of the CO and IR luminosity distributions of the population. In contrast to what was found for F10214, we find that the properties (e.g., FWHM of the CO line profile, M_{gas} , and SFE) of SMM J0939 are similar to the statistical means, except for the SFR, which is lower by a factor of ~ 1.5 , but is nevertheless consistent within the measurement uncertainties. We thus find that the gas mass in SMM J0939 is consistent with other type-2 quasars.

While the gas mass in SMM J0939 is slightly lower than the median of SMGs in the B13 sample, we find it to be consistent with other type-2 quasars, suggesting a possible scenario in which a significant fraction of the gas has already been converted into stars and used for fueling the quasar. As such, given the presence of an obscured quasar and the overlap of properties with both type-2 quasar and SMG populations, a physical interpretation might be that SMM J0939 is transitioning from a short, star-bursting phase to an unobscured quasar phase, consistent with the proposed evolutionary link model between dusty starbursts and quasars (e.g., Sanders et al. 1988; Coppin et al. 2008; Simpson et al. 2012).

We thank the referee for providing constructive comments to improve this manuscript. We thank Shane Bussmann for providing the code UVMCMCFIT for lens modeling, sharing the SMA and VLA data, and for helpful discussions; Alex Conley for providing the code MBB_EMCEE for SED fitting. Support for CARMA construction was derived from the Gordon and Betty Moore Foundation, the Kenneth T. and Eileen L. Norris Foundation, the James S. McDonnell Foundation, the Associates of the California Institute of Technology, the University of Chicago, the states of Illinois, California, and Maryland, and the National Science Foundation. Ongoing CARMA development and operations are supported by the National Science Foundation under a cooperative agreement, and by the CARMA consortium universities.

Facilities: CARMA

REFERENCES

- Baldwin, J. E., Boysen, R. C., Hales, S. E. G., et al. 1985, *MNRAS*, 217, 717
- Barger, A. J., Cowie, L. L., Sanders, D. B., et al. 1998, *Nature*, 394, 248
- Begelman, M. C., Blandford, R. D., & Rees, M. J. 1984, *Reviews of Modern Physics*, 56, 255
- Blain, A. W., Smail, I., Ivison, R. J., Kneib, J.-P., & Frayer, D. T. 2002, *Phys. Rep.*, 369, 111
- Bothwell, M. S., Smail, I., Chapman, S. C., et al. 2013, *MNRAS*, 429, 3047 (B13)
- Bouché, N., Cresci, G., Davies, R., et al. 2007, *ApJ*, 671, 303
- Bussmann, R. S., Pérez-Fournon, I., Amber, S., et al. 2013, *ApJ*, 779, 25
- Bussmann, S., Leung, T. K. D., & Conley, A. 2015a, *uvcmcf*, doi:10.5281/zenodo.27357
- Bussmann, R. S., Riechers, D., Fialkov, A., et al. 2015b, *ApJ*, 812, 43
- Carilli, C. L., & Walter, F. 2013, *ARA&A*, 51, 105
- Carlstrom, J. E., Ade, P. A. R., Aird, K. A., et al. 2011, *PASP*, 123, 568
- Casey, C. M. 2012, *MNRAS*, 425, 3094
- Casey, C. M., Narayanan, D., & Cooray, A. 2014, *Phys. Rep.*, 541, 45
- Chabrier, G. 2003, *PASP*, 115, 763
- Chapman, S. C., Blain, A. W., Smail, I., & Ivison, R. J. 2005, *ApJ*, 622, 772
- Cleary, K., Lawrence, C. R., Marshall, J. A., Hao, L., & Meier, D. 2007, *ApJ*, 660, 117
- Cohen, A. S., Lane, W. M., Cotton, W. D., et al. 2007, *AJ*, 134, 1245
- Condon, J. J., Cotton, W. D., Greisen, E. W., et al. 1998, *AJ*, 115, 1693
- Conley, A., Cooray, A., Vieira, J. D., et al. 2011, *ApJ*, 732, L35
- Coppin, K. E. K., Swinbank, A. M., Neri, R., et al. 2008, *MNRAS*, 389, 45
- Danielson, A. L. R., Swinbank, A. M., Smail, I., et al. 2011, *MNRAS*, 410, 1687
- Deane, R. P., Heywood, I., Rawlings, S., & Marshall, P. J. 2013, *MNRAS*, 434, 23
- Dickinson, M., Papovich, C., Ferguson, H. C., & Budavári, T. 2003, *ApJ*, 587, 25
- Dowell, C. D., Conley, A., Glenn, J., et al. 2014, *ApJ*, 780, 75
- Downes, D., & Solomon, P. M. 1998, *ApJ*, 507, 615
- Dunne, L., Eales, S. A., & Edmunds, M. G. 2003, *MNRAS*, 341, 589
- Eales, S., Dunne, L., Clements, D., et al. 2010, *PASP*, 122, 499
- Engel, H., Tacconi, L. J., Davies, R. L., et al. 2010, *ApJ*, 724, 233
- Fanaroff, B. L., & Riley, J. M. 1974, *MNRAS*, 167, 31P
- Frayer, D. T., Ivison, R. J., Scoville, N. Z., et al. 1998, *ApJ*, 506, L7
- Gavazzi, R., Cooray, A., Conley, A., et al. 2011, *ApJ*, 738, 125 (G11)
- Genzel, R., Tacconi, L. J., Gracia-Carpio, J., et al. 2010, *MNRAS*, 407, 2091
- Greve, T. R., Bertoldi, F., Smail, I., et al. 2005, *MNRAS*, 359, 1165
- Haas, M., Leipski, C., Barthel, P., et al. 2014, *ApJ*, 790, 46 (H14)
- Hales, S. E. G., Waldram, E. M., Rees, N., & Warner, P. J. 1995, *MNRAS*, 274, 447
- Hardcastle, M. J., & Looney, L. W. 2008, *MNRAS*, 388, 176
- Harrison, C. M., Simpson, J. M., Stanley, F., et al. 2015, *ArXiv e-prints*, arXiv:1510.06740
- Hinshaw, G., Larson, D., Komatsu, E., et al. 2013, *ApJS*, 208, 19
- Hodge, J. A., Carilli, C. L., Walter, F., Daddi, E., & Riechers, D. 2013, *ApJ*, 776, 22
- Hodge, J. A., Riechers, D., Decarli, R., et al. 2015, *ApJ*, 798, L18
- Hughes, D. H., Serjeant, S., Dunlop, J., et al. 1998, *Nature*, 394, 241
- Ivison, R. J., Papadopoulos, P. P., Smail, I., et al. 2011, *MNRAS*, 412, 1913
- Ivison, R. J., Swinbank, A. M., Swinyard, B., et al. 2010, *A&A*, 518, L35
- Kellermann, K. I., & Pauliny-Toth, I. I. K. 1973, *AJ*, 78, 828
- . 1981, *ARA&A*, 19, 373
- Kellermann, K. I., Pauliny-Toth, I. I. K., & Williams, P. J. S. 1969, *ApJ*, 157, 1
- Kennicutt, Jr., R. C. 1998, *ARA&A*, 36, 189
- Kirkpatrick, A., Pope, A., Sajina, A., et al. 2015, *ApJ*, 814, 9
- Lagache, G., Puget, J.-L., & Dole, H. 2005, *ARA&A*, 43, 727
- Laing, R. A., & Peacock, J. A. 1980, *MNRAS*, 190, 903
- Meisenheimer, K., Roser, H.-J., Hiltner, P. R., et al. 1989, *A&A*, 219, 63
- Michałowski, M. J., Watson, D., & Hjorth, J. 2010, *ApJ*, 712, 942
- Mullaney, J. R., Alexander, D. M., Goulding, A. D., & Hickox, R. C. 2011, *MNRAS*, 414, 1082
- Mullin, L. M., Hardcastle, M. J., & Riley, J. M. 2006, *MNRAS*, 372, 113
- Negrello, M., Hopwood, R., De Zotti, G., et al. 2010, *Science*, 330, 800
- Neri, R., Genzel, R., Ivison, R. J., et al. 2003, *ApJ*, 597, L113
- Netzer, H., Lutz, D., Schweitzer, M., et al. 2007, *ApJ*, 666, 806
- Oliver, S. J., Bock, J., Altieri, B., et al. 2012, *MNRAS*, 424, 1614
- Pauliny-Toth, I. I. K., Wade, C. M., & Heeschen, D. S. 1966, *ApJS*, 13, 65
- Polletta, M., Nesvadba, N. P. H., Neri, R., et al. 2011, *A&A*, 533, A20

³ Note that Deane et al. (2013) suggest a magnification factor of $\mu_L = 6 \pm 1.5$ for the CO emission in F10214.

- Rengelink, R. B., Tang, Y., de Bruyn, A. G., et al. 1997, *A&AS*, 124, 259
- Riechers, D. A., Walter, F., Carilli, C. L., et al. 2006, *ApJ*, 650, 604
- Riechers, D. A., Hodge, J., Walter, F., Carilli, C. L., & Bertoldi, F. 2011a, *ApJ*, 739, L31
- Riechers, D. A., Carilli, L. C., Walter, F., et al. 2011b, *ApJ*, 733, L11
- Riechers, D. A., Carilli, C. L., Maddalena, R. J., et al. 2011c, *ApJ*, 739, L32
- Riechers, D. A., Cooray, A., Omont, A., et al. 2011d, *ApJ*, 733, L12
- Riechers, D. A., Bradford, C. M., Clements, D. L., et al. 2013, *Nature*, 496, 329
- Sanders, D. B., Soifer, B. T., Elias, J. H., et al. 1988, *ApJ*, 325, 74
- Simpson, J. M., Smail, I., Swinbank, A. M., et al. 2012, *MNRAS*, 426, 3201
- . 2015, *ApJ*, 799, 81
- Smail, I., Ivison, R. J., & Blain, A. W. 1997, *ApJ*, 490, L5
- Smolčić, V., & Riechers, D. A. 2011, *ApJ*, 730, 64
- Solomon, P. M., & Vanden Bout, P. A. 2005, *ARA&A*, 43, 677
- Swinbank, A. M., Smail, I., Longmore, S., et al. 2010, *Nature*, 464, 733
- Swinbank, A. M., Papadopoulos, P. P., Cox, P., et al. 2011, *ApJ*, 742, 11
- Tacconi, L. J., Neri, R., Chapman, S. C., et al. 2006, *ApJ*, 640, 228
- Tacconi, L. J., Genzel, R., Smail, I., et al. 2008, *ApJ*, 680, 246
- Vieira, J. D., Crawford, T. M., Switzer, E. R., et al. 2010, *ApJ*, 719, 763
- Wilson, R. W., Jefferts, K. B., & Penzias, A. A. 1970, *ApJ*, 161, L43

Table 4
Comparison of SMM J0939 with SMGs and type-2 QSOs at $z \sim 2$.

Quantity	Unit	SMM J0939		HLSW-01		Cosmic Eyelash		SMGs		Type-2 QSOs	
				Reference	Reference			Reference			
z		2.221	2.957	R11	S10	2.326	S10	2.2 ^a	2.27 ± 0.32 ^a		
μ_L		10.1 ± 1.4	10.9 ± 0.7	G11	S11	37.5 ± 4.5	S11	—	—		
S_{250}		440 ± 15 ^b	425 ± 10	C11	I10	366 ± 55	I10	—	—		
$I_{CO(3-2)}$	mJy km s ⁻¹	12.6 ± 2.0	9.7 ± 0.5	R11	D11	13.2 ± 0.1	D11	—	—		
Δv_{FWHM}	km s ⁻¹	546 ± 36 ^c	350 ± 25 ^c	R11	D11	< 800 ^{c,d}	D11	550 ± 90 ^e	450 ± 180 ^f		
$L'_{CO(1-0)}$	10 ¹⁰ K km s ⁻¹ pc ²	3.4 ± 0.7	4.2 ± 0.4	R11	D11	1.7 ± 0.2	D11	5.2 ± 1.0	3.0 ^e		
M_{gas}^g	10 ¹⁰ M_\odot	2.7 ± 0.6	3.3 ± 0.3	R11	S10	1.6 ± 0.1	S10	4.2 ± 0.8	2.4 ± 1.4		
L_{FIR}	10 ¹² L_\odot	5.3 ± 0.7	11.0 ± 0.9	C11	I10	1.8 ± 0.2	I10	6.0 ± 0.6 ^h	2.8 ⁱ		
M_{dust}	10 ⁸ M_\odot	5.2 ± 2.1	1 - 5.2	R11	I10	~ 4.0	I10	5.4 ± 1.5 ^{i,j}	...		
SFR _{FIR} ^k	M_\odot yr ⁻¹	526 ± 73	1430 ± 160	C11	I10	~ 235	I10	600 ± 60 ⁱ	855 ± 480		
τ_{depl}	Myr	52 ± 8	23 ± 3	R11	LR16	68 ⁱ	LR16	70 ± 15 ⁱ	35 ⁱ		
$f_{gas-dust}$		55 ± 24	60 - 330	R11	I10	~ 40	I10	78 ± 26 ⁱ	...		
SFE	L_\odot (K km s ⁻¹ pc ²) ⁻¹	256 ± 41	340 ± 40	R11	LR16	135 ± 20 ⁱ	LR16	182 ± 38 ⁱ	347 ± 268		
M_{dyn}	10 ¹⁰ M_\odot	7.8 ± 2.8	3.7 ± 1.8 ^{i,l}	LR16	S11	6.0 ± 0.5	S11	7.2 ± 1.3	...		
$f_{gas-dyn}$		0.4 ± 0.1	0.9 ⁱ	LR16	S11	0.6 ± 0.1	S11	0.6 ± 0.2	...		

References. — C11 = Conley et al. (2011); D11 = Danielson et al. (2011); G11 = Gavazzi et al. (2011); I10 = Ivison et al. (2010); LR16 = this work; R11 = Riechers et al. (2011b); S11 = Swinbank et al. (2011); S10 = Swinbank et al. (2010)

Note. — Properties of SMGs and type-2 QSOs are based on the results from B13 and Polletta et al. (2011), respectively. Gas mass is estimated based on the lowest- J CO line measurements available. Thermalized excitation (i.e., $R_{31} = 1$) has been assumed for type-2 QSOs and the excitation conditions for SMGs are based on CO SLED modeling (see Bothwell et al. 2013). Values listed from row 6 onwards are lensing-corrected, and the errors quoted for SMM J0939 includes uncertainties in μ_L .

^a Statistical average in the sample

^b H14

^c CO($J = 3 \rightarrow 2$)

^d Estimated from Figure 1 in D11

^e Based on CO($J = 3 \rightarrow 2$) and CO($J = 4 \rightarrow 3$) line observations

^f Based on CO($J = 2 \rightarrow 1$), CO($J = 3 \rightarrow 2$), and CO($J = 4 \rightarrow 3$) line observations

^g $\alpha_{CO} = 0.8 M_\odot$ (K km s⁻¹ pc²)⁻¹

^h Inferred from radio continuum measurements via the FIR-radio correlation (B13)

ⁱ Derived from the reported values

^j Using $S_{850\mu m}$ and optically thin, Rayleigh-Jeans approximation (?)

^k Chabrier IMF

^l Using the physical size of CO($J = 5 \rightarrow 4$) emission (G11)

APPENDIX

We perform SED fitting to the (sub)-mm data of SMM J0939 using `MBB_EMCEE` (see §4.2.2). This code uses MCMC to sample the parameter spaces, the total IR luminosity and dust mass are then derived from the set of parameters that maximizes the likelihood. We show in Figure 5 the resulting correlation plots of each pair of parameters (off-diagonals) as well as the marginalized PDFs of each parameter (diagonals) for the fitted optically thick and optically thin models. The parameter values corresponding to the most likely solution are denoted as black crosses in the joint probability distribution plots, and vertical lines in the marginalized PDF plots.

The PDFs of the parameters in the optically thin models are shown in the right panel of Figure 5, the dust emissivity index (β) is highly anti-correlated with the observed-frame dust temperature ($T/(1+z)$), and the marginalized PDFs of all parameters are well-approximated by Gaussians — the best-fit solution is prominent. We note that the best-fit emissivity in this model is unusually low among high-redshift galaxies ($\beta = 0.7_{-0.3}^{+0.2}$, cf. 1–2.5; e.g., Casey 2012, and references therein). While this directly affects the slope of the Rayleigh-Jeans tail of the modified blackbody function, such low emissivity has insignificant impact on the inferred IR luminosity. Despite the factor of ~ 2 difference in dust mass between models, the derived IR luminosities are comparable. As such, we find no evidence of correlation between the inferred dust mass and IR luminosity.

A comparison of the reduced χ^2 between the two models suggests that the optically thick model fit is superior to the optically thin model fit. In the preferred model, the marginalized PDF of the dust emissivity index is highly non-Gaussian, with a noticeably broad distribution across the allowed range (upper limit: 2.2). We therefore fit a second optically thick model, changing the upper limit of β to 3.0. The difference in each parameter of the best-fit solution between these two scenarios is less than 3%, except for the dust mass, which is boosted by a factor of ~ 2 . This is unsurprising given the dearth of data in the rest-frame FIR wavebands, leading to a weakly constrained emissivity, and thus, inferred dust mass. In our analysis, we employ the best-fit parameters and the corresponding inferred properties (dust mass, and IR luminosity) from the former, where a tighter constraint is imposed on β .

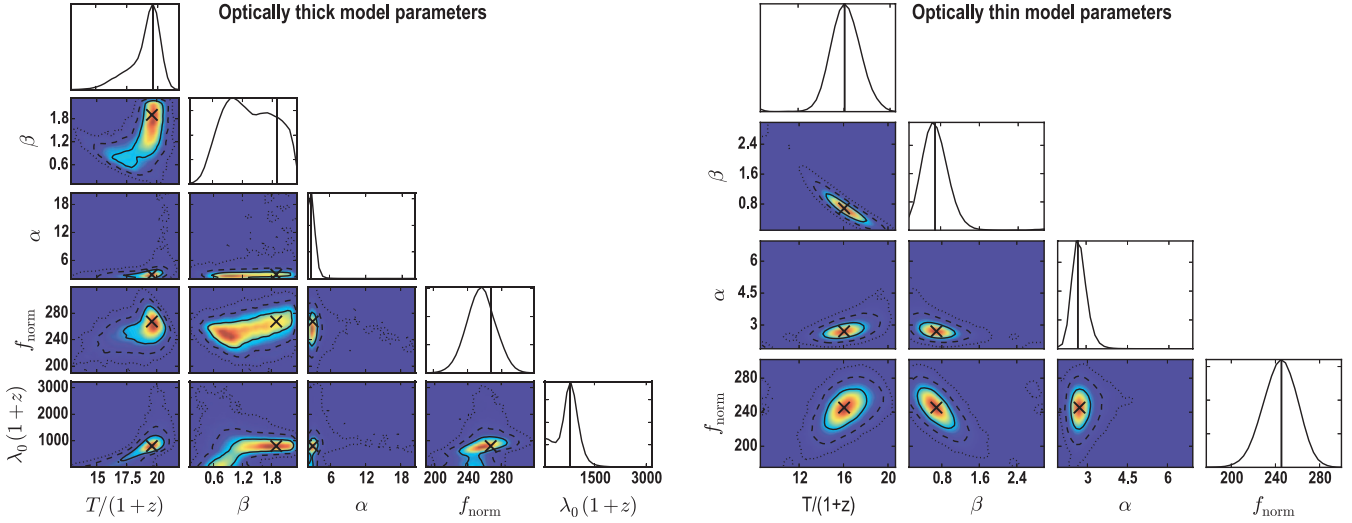


Figure 5. Correlation plots from the fitted SEDs, using optically thick models (left), and optically thin models (right). Marginalized posterior probability distributions of each parameter are plotted along the diagonals, where the solid black vertical lines indicate the set of parameter values that maximizes the likelihood. The joint PDFs between parameters are plotted as 2D histograms on the off-diagonals, where the black crosses denote the locations of the most likely solution in the parameter space. The solid, dashed, and dotted lines correspond to 1σ , 2σ , and 3σ , respectively.